Journal of Rock Mechanics and Geotechnical Engineering 15 (2023) 814–825

Contents lists available at ScienceDirect

Journal of Rock Mechanics and Geotechnical Engineering

journal homepage: www.jrmge.cn

Full Length Article

Mechanical and hydraulic properties of carbonate rock: The critical role of porosity

Kam Ng [a,*], J. Carlos Santamarina [b]

[a] Department of Civil and Architectural Engineering and Construction Management, University of Wyoming, Laramie, WY, 82071, USA
[b] Physical Science and Engineering Division, King Abdullah University of Science and Technology, Thuwal, 23955-6900, Saudi Arabia

ARTICLE INFO

Article history:
Received 26 February 2022
Received in revised form
4 May 2022
Accepted 17 July 2022
Available online 6 September 2022

Keywords:
Rock porosity
Carbonate permeability
Rock unconfined stiffness
Unconfined compressive strength (UCS)

ABSTRACT

Carbonate rocks are extensively used in civil infrastructure and play a critical role in geoenergy geoengineering, either as hydrocarbon reservoirs or potential repositories for CO_2 geological storage. Carbonate genesis and diagenetic overprint determine the properties of carbonate rocks. This study combines recent data gathered from Madison Limestone and an extensive dataset compiled from published sources to analyze the hydraulic and mechanical properties of limestone carbonate rocks. Physical models and data analyses recognize the inherently granular genesis of carbonate rocks and explain the strong dependency of physical properties on porosity. The asymptotically-correct power model in terms of $(1\text{-}\phi/\phi^*)^{\alpha}$ is a good approximation to global trends of unconfined stiffness E and unconfined compressive strength UCS, cohesive intercept in Mohr-Coulomb failure envelopes, and the brittle-to-ductile transition stress. This power model is the analytical solution for the mechanical properties of percolating granular structures. We adopted a limiting granular porosity $\phi^* = 0.5$ for all models, which was consistent with the loosest packing of monosize spheres. The fitted power model has exponent $(\alpha = 2)$ in agreement with percolation theory and highlights the sensitivity of mechanical properties to porosity. Data and models confirm a porosity-independent ratio between unconfined stiffness and strength, and the ratio follows a log-normal distribution with mean $(E/UCS) \approx 300$. The high angle of internal shear strength measured for carbonate rocks reflects delayed contact failure with increased confinement, and it is not sensitive to porosity. Permeability spans more than six orders of magnitude. Grain size controls pore size and determines the reference permeability k^* at the limiting porosity $\phi^* = 0.5$. For a given grain size from fine to coarse-grained dominant carbonates, permeability is very sensitive to changes in porosity, suggesting preferential changes in the internal pore network during compaction.

1. Introduction

Carbonate bio-genesis and post-depositional compaction, crushing, dissolution, and remineralization combine to define the porosity, fabric and inherent heterogeneity of carbonate rocks. In turn, these micro-scale characteristics affect flow and all physico-mechanical properties including stiffness, strength and brittleness. Carbonate heterogeneity and variable engineering properties challenge the design and construction of civil infrastructure and lead to conservative approaches. For example, the capacity of driven piles resting on soft carbonate rocks is usually underpredicted during the design stage, leading to large discrepancies between estimated and measured pile resistances (Ng et al., 2015; Ng and Sullivan, 2017).

Carbonates play an important role in energy geoengineering as well. In fact, carbonate reservoirs contain half of the world's proven oil reserves and contribute 60% of the total oil and gas production worldwide. The regimes in the Middle East (e.g. Saudi Arabia, Libya), Europe (e.g. Russia), Asian (e.g. Republic of Kazakhstan), and North America, host some of the largest carbonate reservoirs (Roehl and Choquette, 1985; Shepherd, 2009). Heterogeneity and associated uncertainty in mechanical and fluid flow properties affect drilling operations, reservoir modeling, production management, and optimization.

* Corresponding author.
E-mail address: kng1@uwyo.edu (K. Ng).
Peer review under responsibility of Institute of Rock and Soil Mechanics, Chinese Academy of Sciences.

https://doi.org/10.1016/j.jrmge.2022.07.017

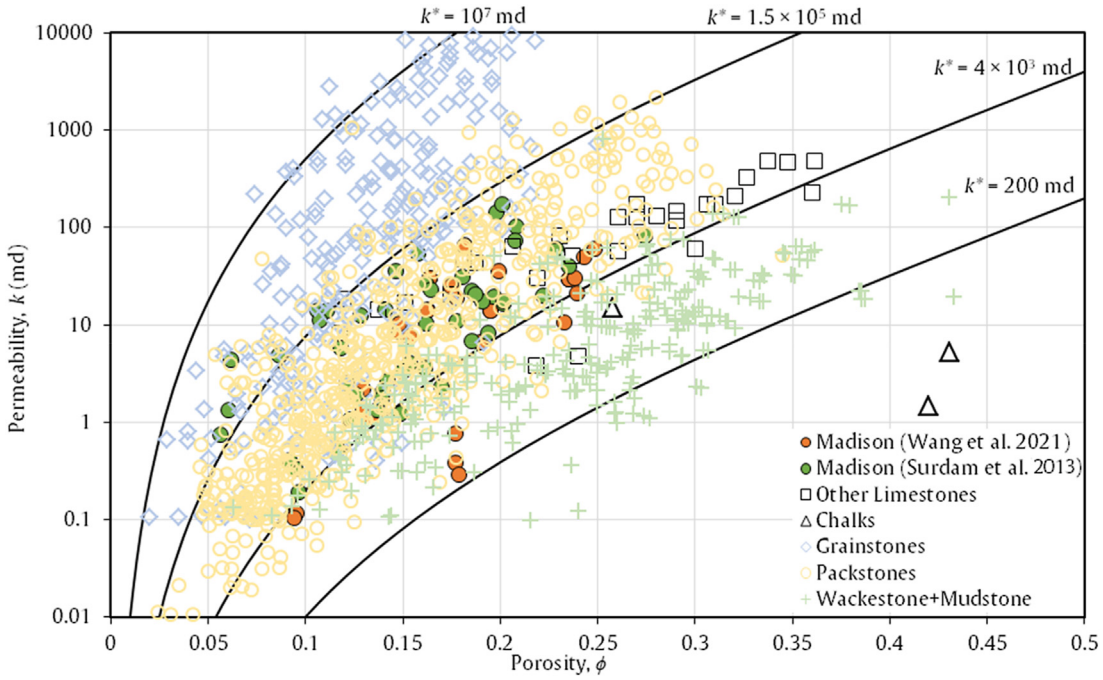

Fig. 1. Permeability versus porosity. Data sources: databases in Lucia (1995), Lindsay et al. (2006), and Cardona and Santamarina (2020); new data from Fabre and Gustkiewicz (1997), Vanorio and Mavko (2011), Surdam et al. (2013), Wang (2017), Yu (2018), and Wang et al. (2021). Trends shown as continues lines correspond to Eq. (1) for the same exponent $\beta = 4.5$; the reference permeabilities k^* correspond to porosity $\phi^* = 0.5$.

More recently, porous carbonate rocks have been considered as candidate repositories for CO_2 geological storage. This is the case of the Rock Springs Uplift in southwest Wyoming, USA (Surdam and Jiao, 2007) where the 76-m thick high-porosity Mississippian Madison Limestone sits beneath the low-permeability Cretaceous shale seal. Spatial variability and heterogeneity were detected during the extensive characterization program of the Madison Formation (Surdam et al., 2013; Shafer, 2013; Wang, 2017; Yu et al., 2019; Ng et al., 2019; Wang et al., 2021). These characteristics must be properly considered in the design of drilling and injection operations to anticipate flow and storativity.

The study combines recent data gathered from Madison Limestone and an extensive dataset compiled from published sources for carbonates around the world. We emphasized porosity as a valuable index property to assess spatial variability and to obtain first-order estimates of material properties in order to guide field characterization and design strategies. Clearly, a more detailed analysis would require pore-scale information related to the geometry of pores and the nature of interparticle bonding. As porosity is systematically reported in the literature, it is available for all carbonates in our database.

We tried to improve our understanding and estimation of permeability, unconfined stiffness and strength, stress-dependent strength, and confining stress at the brittle-to-ductile transition. Observations and analyses recognize the inherent granular genesis of carbonates (applied to all carbonates, from grainstones to mudstones), and build on contact mechanics and percolation theory, rather than on pore-fracture analyses.

2. Porosity and permeability

Carbonate genesis and diagenetic overprint often produce complex multi-scale pore structures that can vary from the submicron scale intraparticle/interparticle/moldic pores to kilometer-scale cave systems (Saller et al., 1994; Mazzullo, 2004; Moh'd, 2009; Moore and Wade, 2013; Head and Vanorio, 2016). Interconnected interparticle pores govern permeability. Together, porosity and permeability determine injectibility, storativity and recovery (Dullien, 1992; Tiab and Donaldson, 2012).

Our database of porosity and permeability combines data gathered in our laboratories and reported in the literature including databases in Lucia (1995) and Lindsay et al. (2006). Fig. 1 shows that carbonate permeability spans more than six orders of magnitude. Given the highly variable interconnected porous network in carbonate rocks, correlations between porosity ϕ and permeability k are weak.

Narrower estimates of permeability involve pore-scale information, such as pore size distribution (PSD) and pore geometry (Clerke, 2009; Buiting and Clerke, 2013). In fact, the permeability of carbonates depends on the largest interconnected pores, so it correlates best with the pore diameter that corresponds to the 80th percentile in pore-size distributions (Cardona and Santamarina, 2020).

Pore-size is a function of (a) grain size as shown in Fig. 1 where permeability is highest in grainstones and lowest in mudstones; and (b) packing density. In general, granular packings exhibit a linear relationship between permeability k and void ratio $e = \phi/(1\text{-}\phi)$ in log-log scale, in agreement with models of fluid flow in porous media (see data and analyses in Ren and Santamarina (2017)). Mathematically, this implies:

$$\frac{k}{k^*} = \left(\frac{e}{e^*}\right)^{\beta} \Rightarrow k = k^*\left(\frac{\phi}{1-\phi}\right)^{\beta} \tag{1}$$

where k^* and e^* are reference values, β is the exponent value.

The second expression in Eq. (1) is obtained for a reference void ratio $e^* = 1$ with a corresponding porosity $\phi^* = e^*/(1+e^*) = 0.5$ that resembles the porosity of a simple cubic packing of monosized particles with $\phi_{sc} = 0.476$. The lines superimposed on Fig. 1 are computed with Eq. (1) for a typical exponent $\beta = 4.5$. It can be

Table 1
Database of uniaxial compressive test results of dry carbonates compiled from published literature.

Carbonate	Location	Number of Tests	Percent calcite (%)	ϕ	ρ_b (g/cm^3)	*UCS* (MPa)	*E* (GPa)	υ	Source
Madison	WY, USA	17	98	0.065–0.08$^{\$}$	2.49–2.53	27–77	NA	NA	Surdam et al. (2013)
Indiana	IN, USA	4	99.6	0.153–0.17$^{\#}$	2.23–2.26	44–59.3	29–29.6	0.18–0.2	Chitty et al. (1994); Prasad et al. (2009)
Fusselman	TX, USA	1	97	0.03$^{\#}$	2.55	39	NA	NA	Handin and Hager (1957)
Wolfcamp	NM, USA	1	96	0.042$^{\#}$	2.63	111	NA	NA	Handin and Hager (1957)
Carthage	MI, USA	1	99.9	0.017$^{\#}$	2.62	89	71.6	NA	Prasad et al. (2009)
Bina	Israel	18	NA	0.06–0.218$^{\#}$	2.19–2.63	15.4–187	10–60.45	0.15–0.4	Palchik (2010, 2011); Palchik and Hatzor (2000, 2002)
Nekarot	Israel	6	NA	0.076–0.104$^{\#}$	2.42–2.49	141–184	44.4–49	0.23–0.28	Palchik and Hatzor (2002)
Yarka	Israel	4	NA	0.157–0.179$^{\#}$	2.3–2.36	38.7–71	6.2–8.4	0.15–0.24	Palchik (2010; 2011)
Sakhnin	Israel	3	NA	0.071–0.132$^{\#}$	2.43–2.6	89–144.6	40.7–57.3	NA	Palchik (2011)
Shmone	Israel	1	NA	0.057$^{\#}$	2.64	172.4	54.4	0.28	Palchik (2011)
Yanuach	Israel	1	NA	0.161$^{\#}$	2.35	35	35.4	0.32	Palchik (2011)
Solnhofen	Germany	4	97.9	0.017–0.055$^{\&\#}$	2.08–2.73	277–310	NA	NA	Renner and Rummel (1996); Mogi (1967, 2007); Prasad et al. (2009)
Miocene	Hungary	39	NA	0.114–0.45$^{\#}$	1.52–2.41	3.08–38.8	0.61–21.1	NA	Vasarhelyi (2005)
Devonian	Turkey	21	>91	0.0114–0.0412$^{+\#}$	2.61–2.73	74.2–138.1	16.7–46.8	NA	Zarif and Tugrul (2003); Handin and Hager (1957)
Kirechane	Turkey	7	90–100	0.074–0.182$^{\#}$	2.24–2.71	16.7–21.4	NA	NA	Ceryan et al. (2013)
Cebecikoy	Turkey	3	NA	0.021–0.023$^{\#}$	2.35–2.42	34–38	NA	0.32–0.34	Kurtulus et al. (2016)
Sogucak	Turkey	3	NA	0.02–0.025$^{\#}$	2.2–2.55	28–45	NA	0.29–0.38	Kurtulus et al. (2016)
Hereke	Turkey	8	NA	0.02–0.023$^{\#}$	2.33–2.5	33–40	NA	0.29–0.35	Kurtulus et al. (2016)
Akveren	Turkey	10	NA	0.022–0.026$^{\#}$	2.22–2.33	28–33	NA	0.33–0.38	Kurtulus et al. (2016)
Akiyoshi	Japan	2	NA	0.005; 0.009$^{\#}$	2.71; 2.72	101; 75	NA	NA	Sato et al. (1981)
Soignies	Belgium	2	95	0.004	2.7	139; 170	NA	NA	Descamps et al. (2011)
Moca	Belgium	1	98.5	0.08	2.65	79	NA	NA	Descamps et al. (2011)
Asmari	Iran	63	93.4	0.0037–0.225$^{\#}$	2.1–2.7	25.1–180	4.7–90	NA	Jamshidi et al. (2017); Najibi et al. (2015)
Kingston	Canada	1	92.6	0.006$^{\#}$	2.72	144	90.3	NA	Prasad et al. (2009)

Note: $: Neutron-density porosity logs; #: Gravimetric method; &: Hydrostatic loading method; +: ISRM suggested method; υ: Poisson's ratio; and NA: Not available.

observed that (a) grain size controls the reference permeability k^* at the limiting porosity $\phi^* = 0.5$; (b) the exponent $\beta = 4.5$ is higher than the power coefficients of $\beta = 2$ and 3 proposed in the Kozeny-Carman parallel tube model where $k \propto \phi^3/(1\text{-}\phi)^2$ (Kozeny, 1927; Carman, 1937); and (c) the high sensitivity to porosity points to preferential changes in the internal pore network structure during compaction.

Other factors influence the permeability and its spatial variability, such as mechanically induced changes (confining stress, Brace et al. (1968); deviatoric stress, Zoback and Byerlee (1975)), thermo-hydro-mechanical coupling (Summers et al., 1978), and fracture characteristics (Kranz et al., 1979; Cardona et al., 2021).

3. Unconfined stiffness and strength

Pores and flaws cause stress concentrations, therefore, strength and stiffness correlations often include rock porosity (Palchik and Hatzor, 2000, 2002). From a granular perspective, porosity is an indicator of contact deformation, as in sintered granular materials. In this section, we explored the correlation between porosity, stiffness and strength based on datasets compiled for carbonate formations worldwide. The carbonate formations are mostly limestone with a minimum of 90% calcite. Other formations with missing calcite content are believed to be limestone based on their formation names.

3.1. Unconfined stiffness

Our database contains stress-strain data measured in 142 unconfined compression tests for 12 different carbonate samples. All specimens having a minimum of 90% calcite (i.e. limestones) had a length to diameter ratio of two, and were either air- or oven-dried. All tests were conducted at room temperature (25 °C), subjected to a typical strain rate of about 1×10^{-5}/s, and involved strain gauges mounted directly on rock specimens. Table 1 summarizes the composition, porosity and dry bulk density ρ_b of the dry carbonates in the database. Porosity ϕ values range from 0.004 for Asmari Limestone to 0.45 for a Hungarian Miocene Limestone. Dry bulk densities ρ_b range from 1.52 g/cm^3 to 2.73 g/cm^3 with some limestones approaching the density of calcite 2.71 g/cm^3.

The reported stiffness values in terms of Young's modulus vary from $E = 0.61$ GPa for the Hungarian Miocene Limestone to $E = 90.3$ GPa for the Kingston Limestone. Genesis, post-depositional burial and diagenesis, and exhumation effects contribute to the observed wide range in stiffness. Fig. 2a shows the inverse relationship between Young's modulus E and porosity ϕ values observed in the database. We adopted an asymptotically-correct power function to satisfy the following limits: (a) stiffness tends to $E \rightarrow E_0$ (GPa) as porosity $\phi \rightarrow 0$; and (b) there is virtually no stiffness in the initial granular packing with limiting porosity ϕ^* before burial and diagenesis. This limiting porosity ϕ^* can be related to the concept of critical porosity ϕ_c that separates two domains: a continuous frame-supported rock medium with $\phi < \phi_c$ and fluid-supported solid suspensions with $\phi > \phi_c$ (Nur et al., 1998). However, very few studies investigate the ϕ_c for carbonate rocks (Fournier and Borgomano, 2009), and the $\phi_c = 0.4$ suggested for carbonate rocks by Nur et al. (1998) is close to the $\phi^* = 0.5$ based on a simple cubic packing of monosized particles. Then, we have

$$E = E_0\left(1 - \frac{\phi}{\phi^*}\right)^{\alpha} = 30\,(1 - 2\phi)^2 \tag{2}$$

The second equality in Eq. (2) shows the fitted trend superimposed on Fig. 2a with the asymptotic value $E_0 = 30$ GPa. Nonlinear equations were fit using the statistical software RStudio to determine the asymptote and the exponent (R Core Team, 2016).

Results in Fig. 2a support the following observations: (a) the mean stiffness at zero porosity $E_0 = 30$ GPa is significantly lower than the stiffness of a single calcite crystal due to the presence of crystal boundaries and impurities at contacts (single crystal: 60–

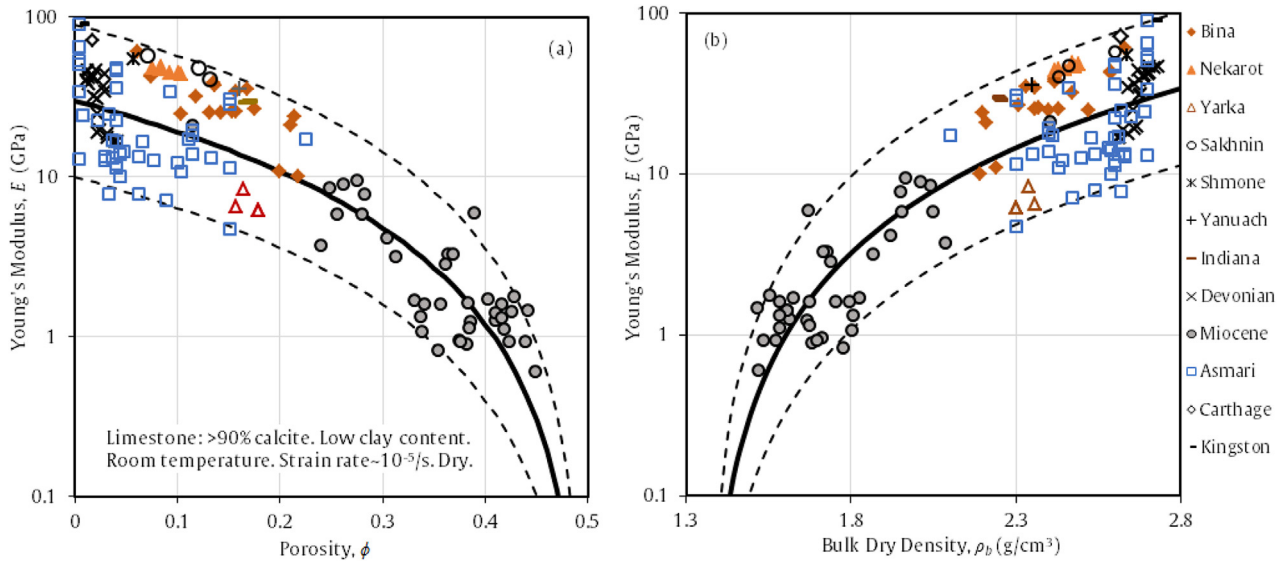

Fig. 2. Young's modulus under unconfined conditions. (a) As a function of porosity: mean trend $E = 30(1-2\phi)^2$. (b) As a function of bulk dry density: mean trend $E = 30\left(\frac{2\rho_b}{2.71}-1\right)^2$. In both cases, the lower and upper bounds are shown in dashed lines and correspond to $E_0 = 10$ GPa and $E_0 = 90$ GPa, respectively.

70 GPa, see Beiki et al., 2013); (b) the limiting porosity of a granular packing $\phi^* \approx 0.5$ is an adequate upper bound; and (c) the exponent $\alpha = 2$ captures the sensitivity of stiffness to porosity. For a given porosity, the variability in stiffness among different carbonate formations in the database reflects the differences in formation history and geological processes such as compaction, dissociation, precipitation, and pore topology (Roehl and Choquette, 1985; Mazzullo et al., 1992; Durrast and Siegesmund, 1999).

Porosity ϕ is a function of the rock dry bulk density ρ_b (g/cm^3) and the mineral density ρ_m (g/cm^3). Then, we can relate stiffness to dry bulk density, from Eq. (2):

$$E = E_0\left(2\frac{\rho_b}{\rho_m}-1\right)^{\alpha} = 30\left(\frac{2\rho_b}{2.71}-1\right)^2 \quad (3)$$

The second equality in Eq. (3) shows the fitted trend with assumed values $\phi^* = 0.5$ and $\rho_m = 2.71$ g/cm^3 for calcite (Fig. 2b).

3.2. Unconfined compressive strength database

The initial porosity plays a prevalent role on the unconfined compressive strength (UCS) of cohesive media, including carbonate rocks (Rzhevsky and Novick, 1971; Farquhar et al., 1994; Chang, 2004; Faÿ-Gomord et al., 2016; Astorqui et al., 2017; Maryam et al., 2018). The mean grain size and mineralogy have a secondary effect on strength, except for low-porosity homogenous carbonates (Chang et al., 2006; Moh'd, 2009; Asef and Farrokhrouz, 2010; Jensen et al., 2010).

The database compiled for this study contains 221 UCS values gathered from 24 different dry limestone samples at 13 locations from around the world (Table 1). Data show a range from $UCS = 3.08$ MPa for the Hungarian Miocene Limestone to $UCS = 310$ MPa for Solnhofen Limestone. Data trends in Fig. 3a confirm the inverse relationship between UCS and ϕ. Once again, the data suggest a power function relation between UCS and ϕ (Fig. 3), where the two asymptotes are (a) the rock strength at zero porosity UCS_0; and (b) vanishing strength $UCS \to 0$ as porosity approached the limiting granular porosity $\phi \to \phi^*$.

$$UCS = UCS_0\left(1-\frac{\phi}{\phi^*}\right)^{\beta} = 100\,(1-2\phi)^2 \quad (4)$$

The second equality in Eq. (4) assumes $\phi^* = 0.5$, and the fitted values capture the average strength at zero porosity $UCS_0 = 95$ MPa (see also Beiki et al., 2013). The exponent $\beta = 2$ reflects the high strength sensitivity to porosity. The variability in strength at low porosity points to the differences in mineralogy and the effect of impurities on contact strength. In terms of dry bulk density, Eq. (4) becomes (Fig. 3b):

$$UCS = UCS_0\left(2\frac{\rho_b}{\rho_m}-1\right)^{\beta} = 100\left(\frac{2\,\rho_b}{2.71}-1\right)^2 \quad (5)$$

3.3. Relationship between unconfined stiffness, strength and porosity

Fig. 4 shows a linear relationship between E and UCS, where both parameters increase by two orders of magnitude when porosity decreases from 0.5 to 0. The log-log plot in Fig. 4 allows a clear assembly of the wide range of stiffnesses from 0.61 GPa to 90.3 GPa. Furthermore, the trend is independent of porosity ϕ (Fig. 4 includes 133 entries). Indeed, Eqs. (2) and (4) or Eqs. (3) and (5) predict a porosity-independent linear relation between E and UCS:

$$E = 300UCS \quad (6)$$

The linear relationship is recommended over a power relationship due to its simplicity and comparable prediction. The ratio (E/UCS) follows a log-normal distribution with mean $\mu[\log_{10}(E/UCS)] = 2.46$ and standard deviation $SD[\log_{10}(E/UCS)] = 0.153$; the corresponding factors are 287 for μ, and 202 and 408 for $\mu \pm SD$. The stiffness-strength relationship observed in carbonates resembles that for most solids, where stiffness is 2–3 orders of magnitude larger than strength.

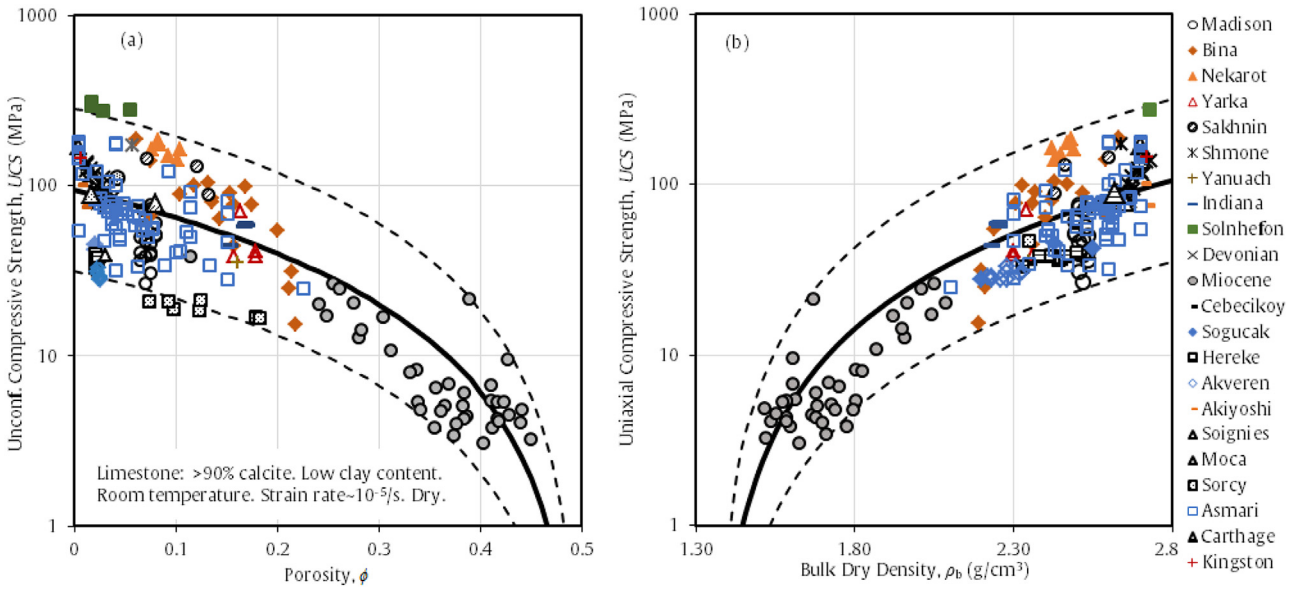

Fig. 3. Unconfined compressive strength. (a) As a function of porosity: mean trend $UCS = 100(1-2\phi)^2$; (b) As a function of bulk dry density: mean trend $UCS = 100\left(\frac{2\rho_b}{2.71}-1\right)^2$. In both cases, the lower and upper bounds are shown in dashed lines and correspond to $UCS_0 = 33$ MPa and $UCS_0 = 300$ MPa, respectively.

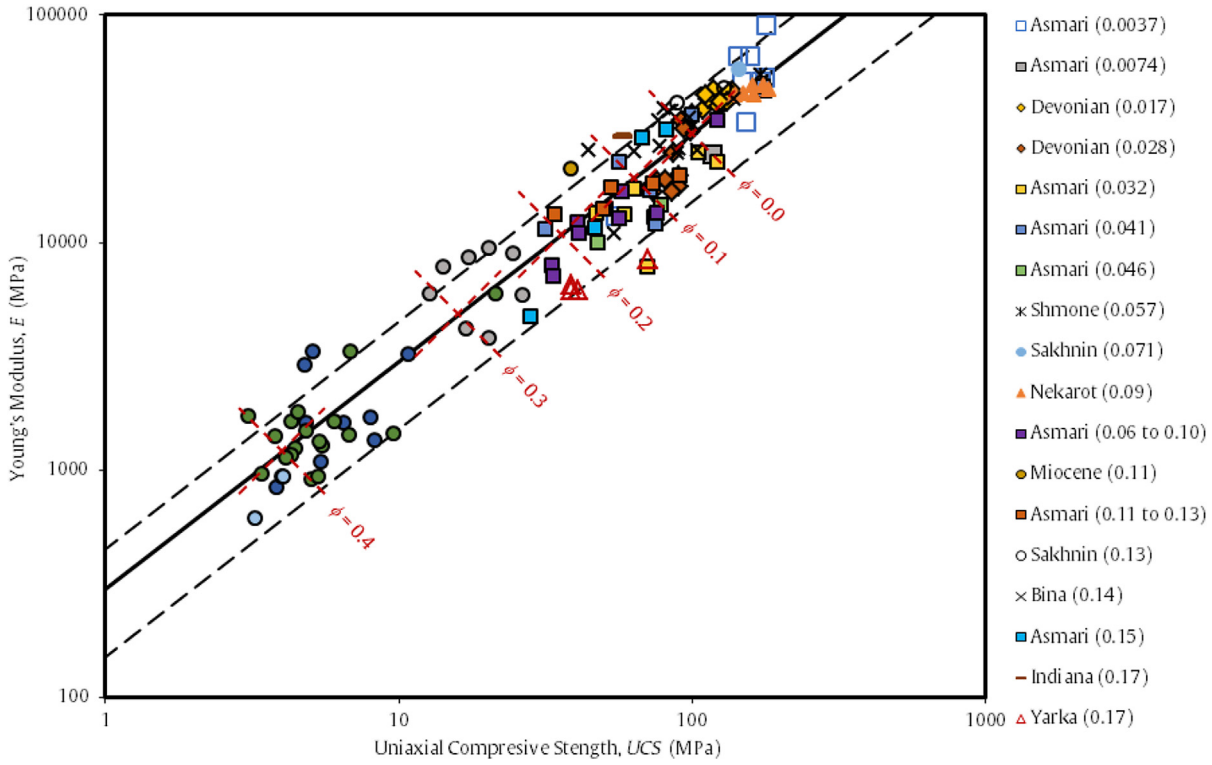

Fig. 4. Young's modulus versus unconfined compressive strength under unconfined conditions. The central trend is $E = 300UCS$. The lower and upper bounds shown in dashed lines correspond to $E = 150UCS$ and $E = 450UCS$. Porosity values of the carbonates are included in the parentheses.

4. Stress-dependent strength and ductility

The previous section addressed unconfined conditions. Rock stiffness and strength are stress-dependent properties (Farquhar, 1993; Vernik et al., 1993). This section explores the effective stress-dependent strength and brittle-to-ductile transition of carbonates.

4.1. Strength

The database compiles 22 triaxial compression test datasets gathered from 15 dry carbonate samples at 10 different locations (Table 2). The minimum calcite component is 90% in all samples, i.e. limestones, except Wolfcamp Limestone from Texas, USA and Saint Maximin Limestone from France. Porosity ϕ values range from

0.003 for Oak Hall Limestone to 0.37 for Saint Maximin Limestone. All triaxial compression data are gathered at room temperature (25 °C).

Data analysis seeks to identify strength parameters, including a link between confined and unconfined strengths. Fig. 5 (inset) shows the Mohr circle from an axial compression triaxial test and the linear Mohr-Coulomb failure envelope both on the normal stress and shear stress plane. The effective normal σ'_f and shear stress τ'_f on the failure plane are a function of the effective major σ'_1 and minor σ'_3 principal stresses and the angle of internal shear strength φ:

$$\sigma'_f = \frac{1}{2}(\sigma'_1 + \sigma'_3) - \frac{1}{2}(\sigma'_1 - \sigma'_3)\sin\varphi = p' - q'\sin\varphi \quad (7)$$

$$\tau'_f = \frac{1}{2}(\sigma'_1 - \sigma'_3)\cos\varphi = q'\cos\varphi \quad (8)$$

where $p' = (\sigma'_1 + \sigma'_3)/2$ and $q' = q = (\sigma'_1 - \sigma'_3)/2$. The Mohr-Coulomb failure criterion relates the normal σ'_f and shear stress τ'_f on the failure plane through the rock cohesion c and the angle of internal shear strength φ.

$$\tau'_f = c + \sigma'_f \tan\varphi \quad (9)$$

Eqs. (7)–(9) are combined to anticipate the relationship between principal stresses at failure:

$$\sigma'_1 = \frac{2c\cos\varphi}{1-\sin\varphi} + \frac{1+\sin\varphi}{1-\sin\varphi}\sigma'_3 \quad (10)$$

The *UCS* is the effective axial stress σ'_1 at failure when $\sigma'_3 = 0$. Then, Eq. (10) predicts:

$$c = UCS\,\frac{1-\sin\varphi}{2\cos\varphi} \quad (11)$$

We used the compiled triaxial dataset to determine the Mohr-Coulomb strength parameters φ and c (Eq. (9), Table 2). The mean angle of internal shear strength is $\varphi = 31°$ for carbonates with a minimum of 90% calcite, i.e. limestone, and a maximum porosity $\phi \le 0.3$ (Note: Saint Maximin Limestone with $\phi = 0.37$ exhibits $\varphi = 14°$). Porosity has a negligible effect on the angle of internal shear strength (see also Scott, 1989).

Fig. 5 shows the cohesive intercept c measured in triaxial tests (red dots) and computed from unconfined compressive strength *UCS* assuming $\varphi = 31°$. The fitted trend parallels with Eq. (4):

$$c = c_0\left(1 - \frac{\phi}{\phi^*}\right)^{\psi} = 80(1-2\phi)^3 \quad (12)$$

The second equality shows the mean trend for a limiting porosity $\phi^* = 0.5$. The mean cohesion at zero porosity c_0 is 80 MPa, and the fitted exponent $\psi = 3$. Analogous to the *UCS*, cohesion c rapidly decreases as porosity tends to $\phi \to \phi^*$. Finally, Eqs. (9) and (12) combine in the following mean failure criterion for carbonates based on the available data:

$$\tau_f = 80(1-2\phi)^3 + \sigma_f \tan 31° \quad (13)$$

In terms of the mean effective stress $p' = (\sigma'_1 + \sigma'_3)/2$ and the

Table 2
Database of triaxial compressive test results of dry carbonates compiled from published literature.

Carbonate	Location	Number of tests	Percent Calcite (%)	ϕ	Effective confining stress (MPa)	ε_{max} (%)	Mohr-Coulomb criterion		Failure	Source
							c (MPa)	φ (°)		
Madison	WY, USA	3	98	0.085[$]	17, 35, 55	0.65	7.15	39.4	B; T	Shafer (2013)
Madison[@]	WY, USA	6	98	0.094 −0.23*	7, 35, 55				B; T	Wang (2017), Yu (2018), Ng et al. (2019)
Fusselman	TX, USA	3	97	0.03[@]	0, 101, 203	16	NA	NA	B; T; D	Handin and Hager (1957)
Wolfcamp	TX, USA	3	75	0.042[@]	0, 101, 203	4	NA	NA	B; T; D	Handin and Hager (1957)
Wolfcamp	NM, USA	3	96	0.042[@]	0, 101, 203	9	NA	NA	B; T; D	Handin and Hager (1957)
Oak Hall	PA, USA	8	99	0.003	18, 41, 76, 125, 159, 220, 335, 466	4	109.6	29.3	B; T; D	Byerlee (1968)
Indiana	Indiana, USA	11	99	0.194[@]	0, 7, 14, 21, 28, 34, 41, 48, 55, 62, 69	2.7	9	30.8	B; T; D	Schwartz (1964)
Indiana	Indiana, USA	6	99	0.156[@]	5, 10, 20, 30, 40, 50	3.5	14	27.1	B; T; D	Vajdova et al. (2004)
Soignies	Belgium	5	95	0.004	0, 30, 50, 75, 90	3	52.8	30.4	B; T	Descamps et al. (2011)
Moca	Belgium	8	98.5	0.08	0, 10, 20, 30, 40, 60, 80, 100	3.5	24.4	32.9	B; T; D	Descamps et al. (2011)
Sorcy	Belgium	6	~100	0.30	0, 5, 10, 20, 30, 60	1.5	11.7	29.7	B; T; D	Descamps et al. (2011)
Solnhefon	Germany	6	99	0.03[@]	50, 100, 200, 300, 350, 435	5	76.7	35.5	B; T; D	Baud et al. (2000)
Solnhefon	Germany	7	99	0.048	17, 37, 60, 81, 122, 204, 517	5	81.6	26.9	B; T; D	Byerlee (1968)
Solnhefon	Germany	7	99	0.017[@]	0, 76, 101, 127, 152, 304, 507	1.9	85.1	32.9	B; T; D	Heard (1960)
Solnhefon	Germany	5	99	0.059[@]	100, 200, 400, 600, 800	2	NA	NA	T; D	Edmond and Paterson (1972)
Solnhefon	Germany	8	99	0.015	35, 35, 69, 69, 104, 104, 138, 138	1.4	NA	NA	B; T	Serdengecti and Boozer (1961)
St. Maximin	France	5	61	0.37[@]	3, 5, 6, 9, 12	1.6	5.8	14.1	B; T; D	Baud et al. (2000)
Tavel	France	8	NA	0.104[@]	10, 20, 30, 50, 100, 150, 200, 240	4.6	67.3	22.8	B; T; D	Vajdova et al. (2004)
White Tavel	France	14	99	0.147[@]	0, 20, 20, 35, 35, 55, 55, 55, 70, 70, 70, 85, 85, 85	4.4	10.4	29.8	B; T; D	Nicolas et al. (2016)
Majella	Italy	3	NA	0.32[@]	25, 25, 25	NA	NA	NA	D	Vajdova et al. (2012)
Comiso	Italy	4	97.7	0.101[@]	7, 15, 30, 50	1.3	25.4	36.9	B; T; D	Castagna et al. (2018)
Devonian	Turkey	3	NA	0.023[@]	0, 101, 203	20	NA	NA	B; T; D	Handin and Hager (1957)

Note: ε_{max}: Maximum axial strain attained in percentage at the maximum applied deviator stress; @: Temperature at 93 °C and brine-saturated; *: Gas expansion method; B: Brittle regime; T: Transition regime; and D: Ductile regime.

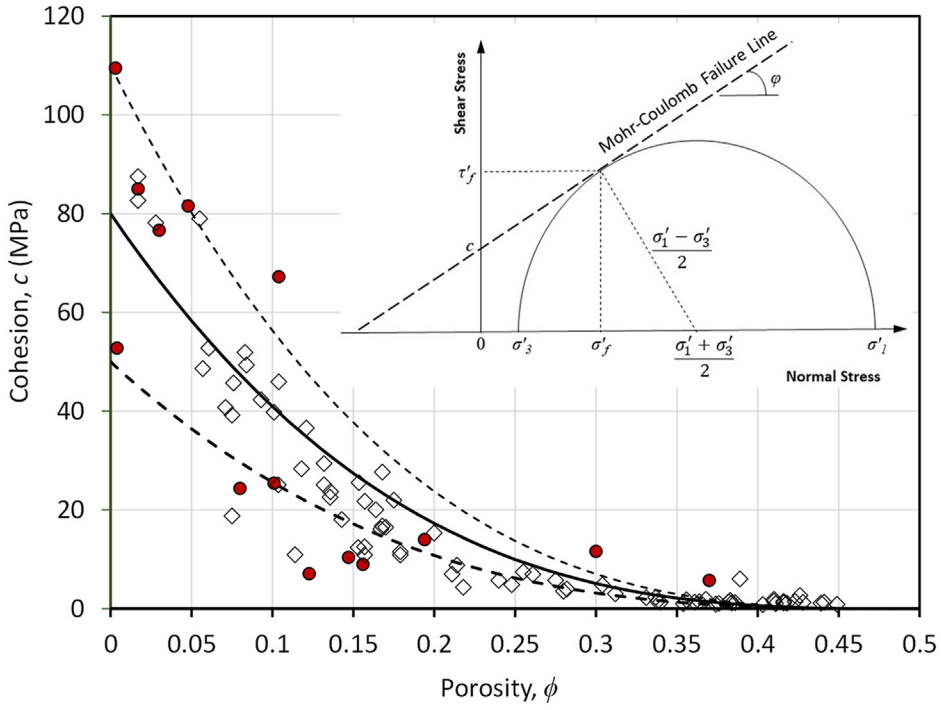

Fig. 5. Mohr-Coulomb failure criterion – Cohesion intercept as a function of porosity. Red dots: Values extracted from sets of triaxial tests. White diamonds: Computed from unconfined compressive strength for mean $\varphi = 31°$. The mean trend is $c = 80(1-2\phi)^3$. The lower and upper bounds shown in dashed lines correspond to $c_0 = 50$ MPa and $c_0 = 110$ MPa, respectively.

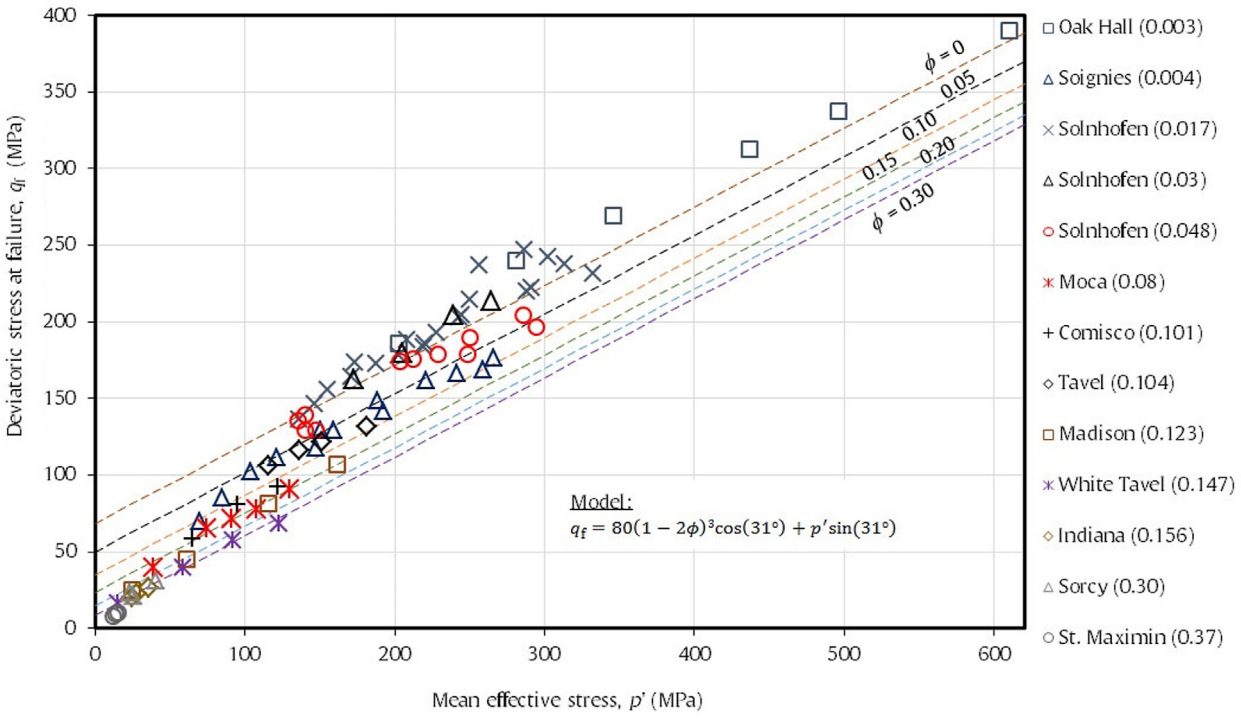

Fig. 6. Mohr-Coulomb failure criterion in q-p' space. Data collected from the literature. All trends computed for the same parameters (Eq. (14)). Porosity values of the carbonates are included in the parentheses.

deviatoric stress at failure $q_f = (\sigma'_1 - \sigma'_3)_{max}/2$, the Mohr-Coulomb failure criterion is

$$q_f = c\cos\varphi + p'\sin\varphi \tag{14}$$

Compiled experimental results lead to the following semi-empirical function for deviatoric stress at failure in terms of the mean effective stress (Eq. (12) and (14)):

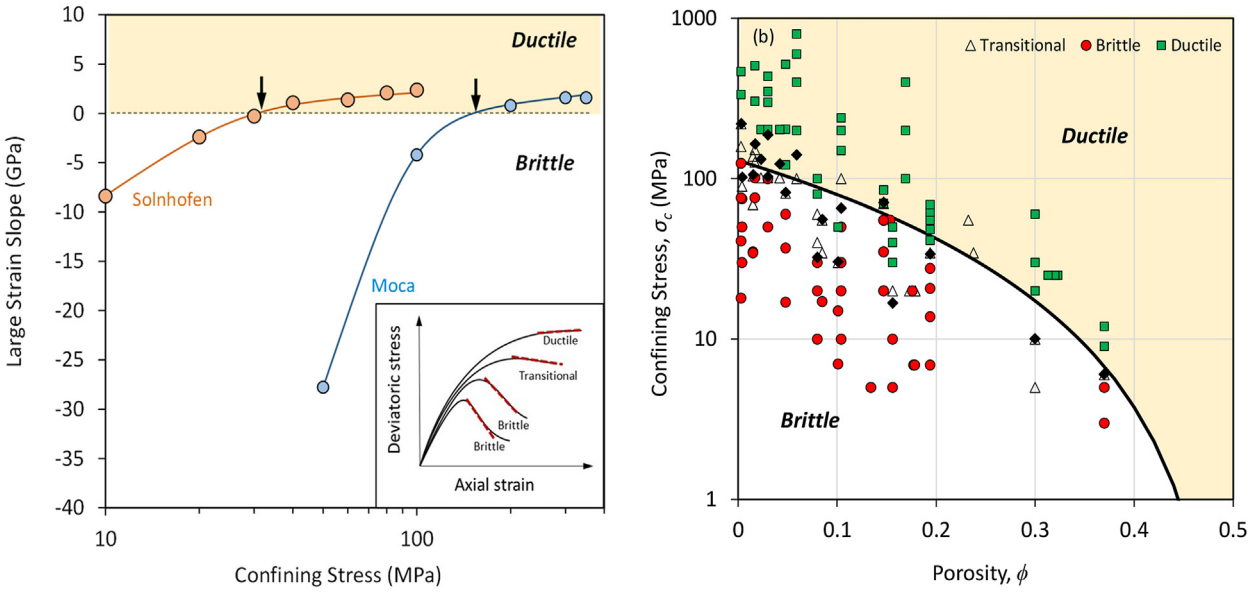

Fig. 7. Brittle-to-ductile transition. (a) determination of the brittle-to-ductile transition using the large strain slope, and (b) Triaxial data versus porosity: single tests and inferred brittle to ductile transition stress (back diamonds). The dividing boundary is $\sigma_{bd} = 130\,(1-2\phi)^{2.2}$.

$$q_f = 80\,(1-2\phi)^3\cos 31^\circ + p'\sin 31^\circ \quad (15)$$

Fig. 6 shows the predicted p' and q_f failure lines using Eq. (15) superimposed on top of triaxial test data gathered for 13 carbonates (porosities ϕ from 0 to 0.37).

4.2. Brittle-to-ductile transition

Rocks subjected to low confinement experience propagation of contact breakage, contiguous damage coalescence, shear localization, dilation and a sudden loss in strength (Brace, 1978; Baud et al., 2000, 2009; Vajdova et al., 2004; Nicolas et al., 2017). However, rocks under high confinement above brittle-to-ductile transition experience shear-enhanced compaction, pore collapse, crystal plasticity, distributed grain debonding and micro-cracking, grain rotation and grain-scale plastic flow (Fredrich et al., 1989; Dresen and Evans, 1993; Renner and Rummel, 1996; Paterson and Wong, 2005; Zhu et al., 2010; Dautriat et al., 2011).

The stress-dependent brittle-to-ductile transition in carbonate rocks follows similar patterns (Renner and Rummel, 1996; Wong et al., 1997; Vajdova et al., 2004; Wong and Baud, 2012; Nicolas et al., 2016). Internally, there is a transition from frictional sliding in brittle failure to cataclastic flow in ductile failure (e.g. Logan, 1987; Wong and Baud, 2012). However, the brittle-to-ductile transition in carbonate rocks is often unclear as these rocks may experience substantial inelastic strain but eventually fail in brittle mode (Jaeger et al., 2007). The extended strain hardening response reflects additional deformation mechanisms in carbonate rocks, including calcite twinning and slip (Turner et al., 1954; Griggs et al., 1960; Fredrich et al., 1989).

There is no standardized protocol to determine the confining stress at the brittle-to-ductile transition σ_{bd}. Previous studies considered the axial stress at volumetric strain reversal (Walton et al., 2017) and the post-yield strength and dilatancy (Wong and Baud, 2012). We followed a simple yet robust approach to estimate the σ_{bd} from stress-strain triaxial data (Fig. 7a): (a) determine the stress-strain slope at large-strain; (b) plot the measured slope against the confining stress; and (c) the brittle-to-ductile transition is the effective confining stress at the zero intercept, where the slope changes from negative "strain-softening" to positive "strain-hardening" (Fig. 7a).

We repeated this methodology for published triaxial datasets obtained for 19 dry carbonates at room temperature 25 °C (Table 2). Fig. 7b shows all test results plotted on a confining stress versus porosity space. Each data point represents a triaxial test: green squares mean ductile strain-hardening response (positive slope), red circles mean brittle post-peak softening response (marked post-peak negative slope), and white triangles mean transitional response.

Black diamonds show the determined σ_{bd} for each dataset following the procedure described above (as in Fig. 7a). σ_{bd} values range from 15.5 MPa for Saint Maximin Limestone to 610 MPa for Oak Hall Limestone (see also: Heard, 1960; Rutter, 1972). Overall, the data suggest that lower-porosity carbonates exhibit brittle-to-ductile transitions at higher confining stresses (see also Logan, 1987). In agreement with models selected above, we used a power model to relate the brittle-to-ductile transition stress σ_{bd} (MPa) to porosity ϕ (solid line in Fig. 7b),

$$\sigma_{bd} = \sigma_0\left(1-\frac{\phi}{\phi^*}\right)^{\xi} = 130(1-2\phi)^{2.2} \quad (16)$$

where σ_0 is confining stress when ϕ approaches zero, and the exponent $\xi = 2.2$.

In this case, the limiting porosity $\phi^* = 0.5$ is in agreement with inherently ductile, very loose granular packing.

5. Physical model analysis

Published empirical models for the hydraulic and mechanical properties of carbonate rocks are either exponential or power functions written in terms of density ρ, porosity ϕ or solidity $\Sigma = 1-\phi$. Table 3 summarizes these models and includes the new relations adopted in this study (Tables 1 and 2).

Previous studies often considered rocks as a continuum where pores and flaws are soft anomalies that cause stress concentrations and act as nucleation sites for fracture initiation and propagation. When tested against our databases, these models show adequate

Table 3
Carbonate rocks: Empirical equations for hydraulic and mechanical properties (See Tables A1 and A2 in Appendix A for details and fitting parameters).

Equations	Source
Permeability k	
$\frac{k}{k^*} = \left(\frac{\phi}{1-\phi}\right)^{\beta}$	This study (limiting granular porosity $\phi^* = 0.5$)
Unconfined stiffness E	
$E = E_0\, e^{-\alpha\phi}$	Farquhar et al. (1994); Ameen et al. (2009); Faÿ-Gomord et al. (2016)
$E = E_0(1-2\phi)^{\alpha} = E_0\left(2\frac{\rho_b}{\rho_m}-1\right)^{\alpha}$	This study (limiting granular porosity $\phi^* = 0.5$)
$E = a' + b\ UCS$	Afsari et al. (2009); Palchik (2011); this study
$E = aUCS^{\theta}\,\phi^{\vartheta}\,d_g^{\omega}$ (Unit of UCS in MPa)	Palchik and Hatzor (2000); Chang (2004); Asef and Farrokhrouz (2010); Najibi et al. (2015)
Unconfined compressive strength UCS	
$UCS = UCS_0\, e^{-\beta\phi}$	Farquhar et al. (1994); Chang (2004); Moh'd (2009); Faÿ-Gomord et al. (2016)
$UCS = UCS_0(1-\phi)^{\beta} = UCS_0\left(\frac{\rho_b}{\rho_m}\right)^{\beta}$	Rzhevsky and Novick (1971); Astorqui et al. (2017)
$UCS = UCS_0(1-2\phi)^{\beta} = UCS_0\left(2\frac{\rho_b}{\rho_m}-1\right)^{\beta}$	This study (limiting granular porosity $\phi^* = 0.5$)
$UCS = a' - b\ln\phi$	Hebib et al. (2017)
$UCS = a' - b\,\phi - c\,\rho + d\,S_w$	Maryam et al. (2018)
Stress at brittle-to-ductile transition σ_{bd}	
$\sigma_{bd} = \sigma_0\left(1-\frac{\phi}{\phi^*}\right)^{\xi} = 130\,(1-2\phi)^{2.2}$	This study (for initial granular porosity $\phi^* = 0.5$)
Confinement-dependent shear strength q_f	
$q_f = c_0(1-2\phi)^{\psi}\cos\varphi + p'\sin\varphi$	This study

Note: d_g: mean grain size; S_w: water saturation; Fitting factors a', b, c, d and exponents α, β, θ, ω, ϑ, ξ.
Sources: Rocks from multiple locations including Algeria, Belgium, France, Iran, Israel, Russia, Saudi Arabia, Spain, United Kingdom, and USA.

trends for low porosity carbonates, but fail to anticipate trends at high porosity.

In fact, the inherent granular genesis of carbonates readily confirmed by SEM images: (a) supports a contact-mechanics based analysis rather than a porous-continuum formulation; (b) enforces a limiting porosity ϕ^* where particles jam and start forming percolating force chains; and (c) implies that mechanical properties P below the percolation porosity $\phi < \phi^*$ follow a power function of the form (Sahimi, 1994; Kovacik, 1999; Nezamabadi et al., 2021; Ternero et al., 2021):

$$P = P_0\left(1-\frac{\phi}{\phi^*}\right)^{\alpha} \tag{17}$$

Indeed, this expression matches trends identified above for all the mechanical parameters. The Taylor expansion of Eq. (17) for $\phi \to 0$ is

$$P = P_0\left(1-\frac{\alpha\,\phi}{\phi^*}\right)^{\alpha} = P_0(1-2\,\alpha\,\phi) \tag{18}$$

where P_0 is the mechanical property at the percolation porosity; the second equality corresponds to $\phi^* = 0.5$. Clearly, we can always approximate trends with a linear relationship near $\phi \to 0$ as adopted in some earlier studies where pore-scale characteristics dominate. On the other hand, percolation and contact mechanics gain relevance at high initial porosities $\phi \to \phi^*$.

The simple cubic packing is the loosest arrangement of monosized spherical particles, thus its porosity $\phi_0 = 0.476$ is an upper bound for the porosity granular materials may attain (Note: there may be intra-particle vuggy porosity in carbonates). This bound is consistent with our database and justifies the adopted limiting porosity $\phi^* = 0.5$. Time and confinement promote contact yield as well as dissolution-precipitation. Under isotropic conditions, the six contacts around a particle flatten and spherical caps at contacts dissolve and re-precipitate coating free surfaces nearby. Spherical caps in x, y, z directions interfere when contact areas reach a radius $a = r\sin 45^\circ$ (r: particle radius). At this point, the remaining pores become isolated and the occluded porosity ϕ is 0.035, as observed in sintered materials in powder metallurgy (see Danninger et al., 1993). Detailed analysis is listed in Appendix A. In fact, most carbonates in our database have porosities between the two boundaries identified above, $0.035 \le \phi \le 0.476$.

The rock strength and stiffness are determined by localized contact deformation and contact strength, which are function of the contact area relative to the total area. A geometric analysis and algebraic manipulations lead to the following relationship between relative contact area A_r and porosity ϕ (see Appendix A)

$$\phi = 1 - \frac{\pi}{2} - 3A_r + \left[3\sqrt{\pi}\left(\frac{1}{\pi + 4A_r}\right)^{3/2}\right]^{-1} \tag{19}$$

Eq. (19) predicts a trend that is very similar to the power function $(1-2\phi)^2$ adopted above for stiffness, strength, and brittle-to-ductile transition (with limiting porosity $\phi^* = 0.5$, Eqs. (2), (4) and (16), see Appendix A). Therefore, contact mechanics determines the small and large strain mechanical properties of carbonates. Note that the relationship between relative contact area A_r and porosity ϕ in Eq. (9) is independent of grain size, as observed in experimental studies reported above.

Rock studies using discrete element simulations with cemented grains show that the brittle-to-ductile transition corresponds to the stress where bond breakage changes from tensile-controlled (at low confinement) to shear-controlled at high confinement (Garcia, 2020). The high angle of internal shear strength observed in carbonates $\varphi \approx 31^\circ$ indicates delayed contact tensile failure with increased confinement (Fig. 6).

6. Conclusions

Results in this context show that the mechanical and hydraulic properties of limestone carbonates reflect their granular genesis and diagenetic overprint and exhibit a strong dependency on porosity. Power functions capture the effect of porosity on unconfined stiffness, compressive strength and the brittle-to-ductile transition stress. The observed power functions $(1\text{-}\phi/\phi^*)^{\alpha}$ agree with percolation theory. We adopted a limiting granular porosity $\phi^* = 0.5$ for all models which is consistent with the loosest packing of monosize spheres. Asymptotes for the mechanical properties at zero porosity are lower than the corresponding mechanical properties for a single calcite crystal due to compliance and the presence of impurities at crystal interfaces. On the other hand, the

unconfined stiffness, compressive strength and brittle-to-ductile transition stress vanish as the limestone carbonate porosity approaches the loosest granular packing $\phi \rightarrow \phi^*$. The fitted power equations have exponents $\alpha = 2$ or greater in agreement with percolation theory, highlighting the sensitivity of mechanical properties to porosity.

The linear relationship between unconfined stiffness E and strength UCS resembles trends observed for a wide range of solids. In the case of limestone carbonates, E/UCS is porosity independent and follows a log-normal distribution with mean $\mu\,(E/UCS) \approx 300$ and standard deviation $SD\,(E/UCS) \approx 100$.

The high angle of internal shear strength measured for limestone carbonates reflects delayed contact failure with increased confinement, and it is not sensitive to porosity. However, the cohesive intercept c decreases with porosity ϕ. Consequently, failure envelopes define parallel lines as a function of porosity in the τ-σ or q-p' spaces.

The permeability of carbonates spans more than six orders of magnitude. Grain size controls pore size and determines the reference permeability k^* at the limiting porosity $\phi^* = 0.5$. For a given grain size from fine to coarse-grained dominant carbonates, permeability k is very sensitive to changes in porosity due to internal changes in pore structure and connectivity.

Declaration of competing interest

The authors declare that they have no known competing financial interests or personal relationships that could have appeared to influence the work reported in this paper.

Acknowledgments

This research was supported by the KAUST Endowment at King Abdullah University of Science and Technology, Saudi Arabia. We thank Gabrielle. E. Abelskamp in Energy GeoEngineering Laboratory at King Abdullah University of Science and Technology for editing the manuscript.

Appendix A. Supplementary data

Supplementary data to this article can be found online at https://doi.org/10.1016/j.jrmge.2022.07.017.

References

Astorqui, J.S.C., Merino, M.d.R., Sáez, P.V., Porras-Amores, C., 2017. Analysis of the relationship between density and mechanical strength of lightened gypsums: proposal for a coefficient of lightning. Adv. Mater. Sci. Eng. 2017, 7092521.
Afsari, M., Ghafoori, M., Roostaeian, M., Haghshenas, A., Ataei, A., Masoudi, R., 2009. Mechanical earth model (MEM): an effective tool for borehole stability analysis and managed pressure drilling (case study). In: Proceeding of the SPE Middle East Oil and Gas Show and Conference, Manama, Bahrain, SPE-118780-MS.
Ameen, S.A., Smart, B.G.D., Somerville, J.M., Hammilton, S., Naji, N.A., 2009. Predicting rock mechanical properties of carbonates from wireline logs (A case study: arab-D reservoir, Ghawar field, Saudi Arabia). Mar. Petrol. Geol. 26 (4), 430–444.
Asef, M.R., Farrokhrouz, M., 2010. Governing parameters for approximation of carbonates UCS. Electron. J. Geotech. Eng. 15, 1581–1592.
Baud, P., Schubnel, A., Wong, T.F., 2000. Dilatancy, compaction, and failure mode in Solnhofen limestone. J. Geophys. Res. Solid Earth 105, 19289–19303.
Baud, P., Vinciguerra, S., David, C., Cavallo, A., Walker, E., Reuschile, T., 2009. Compaction and failure in high porosity carbonates: mechanical data and microstructural observations. Pure Appl. Geophys. 166, 869–898.
Beiki, M., Majdi, A., Givshad, A.D., 2013. Application of genetic programming to predict the uniaxial compressive strength and elastic modulus of carbonate rocks. Int. J. Rock Mech. Min. Sci. 63, 159–169.
Brace, W.F., 1978. Volume changes during fracture and frictional sliding: a review. Pure Appl. Geophys. 116, 603–614.
Brace, W.F., Walsh, J.B., Frangos, W.T., 1968. Permeability of granite under high pressure. J. Geophys. Res. Solid Earth 73, 2225–2236.
Buiting, J.J.M., Clerke, E.A., 2013. Permeability from porosimetry measurements: derivation for a tortuous and fractal tubular bundle. J. Pet. Sci. Eng. 108, 267–278.
Byerlee, J.D., 1968. Brittle-ductile transition in rocks. J. Geophys. Res.: Solid Earth 73, 4741–4750.
Cardona, A., Santamarina, J.C., 2020. Carbonate rocks: matrix permeability estimation. AAPG Bull. 104 (1), 131–144.
Cardona, A., Finkbeiner, T., Santamarina, J.C., 2021. Natural rock fractures: from aperture to fluid flow. Rock Mech. Rock Eng. 54, 5827–5844.
Carman, P.C., 1937. Fluid flow through granular beds. Trans. Inst. Chem. Eng. 15, 150.
Castagna, A., Ougier-Simonin, A., Benson, P.M., et al., 2018. Thermal damage and pore pressure effects of the brittle-to-ductile transition in Comiso limestone. J. Geophys. Res. Solid Earth 123, 7644–7660.
Ceryan, N., Okkan, U., Kesimal, A., 2013. Prediction of unconfined compressive strength of carbonate rocks using artificial neural networks. Environ. Earth Sci. 68, 807–819.
Chang, C., 2004. Empirical rock strength logging in boreholes penetrating sedimentary formations. Geophys. Geophys. Explor. 7 (3), 174–183.
Chang, C., Zoback, M.D., Khaksar, A., 2006. Empirical relations between rock strength and physical properties in sedimentary rocks. J. Pet. Sci. Eng. 51, 223–237.
Chitty, D.E., Blouin, S.E., Sun, X., Kim, K., 1994. Laboratory Investigation and Analysis of the Strength and Deformation of Joints and Fluid Flow in Salem Limestone. Applied Research Associates, Inc., South Royalton, VT, USA. Technical report DNA-TR-93-63.
Permeability, relative permeability, microscopic displacement efficiency and pore geometry of M_1 dimodal pore systems in Arab-D limestone. In: Clerke (Ed.), SPE J. 14 (3), 524–531.
Danninger, H., Jangg, G., Weiss, B., Stickler, R., 1993. Microstructure and mechanical properties of Sintered Iron. Part I. Basic considerations and review of literature. Int. J. Powder Metall. 25, 111–117.
Dautriat, J., Bornert, M., Gland, N., Dimanov, A., Raphanel, J., 2011. Localized deformation induced by heterogeneities in porous carbonate analysed by multi-scale digital image correlation. Tectonophysics 503 (1), 100–116.
Descamps, F., Tshibangu, J.P., Silva, M.R., Verbrugge, J.C., 2011. Behavior of carbonated rocks under true triaxial compression. In: Proceedings of the 12th ISRM Congress on Rock Mechanics. Beijing, China.
Dresen, G., Evans, B., 1993. Brittle and semibrittle deformation of synthetic marbles composed of two phases. J. Geophys. Res. 98, 11921–11933.
Dullien, F.A.L., 1992. Porous Media: Fluid Transport and Pore Structure, second ed. Academic Press, San Diego, CA, USA.
Durrast, H., Siegesmund, S., 1999. Correlation between rock fabrics and physical properties of carbonate reservoir rocks. Int. J. Earth Sci. 88 (3), 392–408.
Edmond, J.M., Paterson, M.S., 1972. Volume changes during the deformation of rocks at high pressure. Int. J. Rock Mech. Min. Sci. 9, 161–182.
Fabre, D., Gustkiewicz, J., 1997. Poroelastic properties of limestones and sandstones under hydrostatic conditions. Int. J. Rock Mech. Min. Sci. 34 (1), 127–134.
Farquhar, R.A., 1993. Petro-mechanical Characterisation of the Rotliegendes Sandstone. PhD Thesis. Heriot-Watt University, Edinburgh, Scotland, UK.
Farquhar, R.A., Somerville, J.M., Smart, B.G., 1994. Porosity as a geomechanical indicator: an application of core and log data and rock mechanics. In: Proceeding of the European Petroleum Conference. London, UK, pp. 481–489.
Faÿ-Gomord, O., Descamps, F., Tshibangu, J., Vandycke, S., Swennen, R., 2016. Unraveling chalk microtextural properties from indentation tests. Eng. Geol. 209, 30–43.
Fournier, F., Borgomano, J., 2009. Critical porosity and elastic properties of microporous mixed carbonate-siliciclastic rocks. Geophysics 74 (2), E93–E109.
Fredrich, J.T., Evans, B., Wong, T.F., 1989. Micromechanics of the brittle to plastic transition in Carrara marble. J. Geophys. Res. 94 (B4), 4129–4145.
Garcia, A., 2020. Thermo-hydro-mechanically Coupled Processes in Fractured Rocks. PhD Thesis. King Abdullah University of Science and Technology, Thuwal, Saudi Arabia.
Griggs, D.T., Turner, F.J., Heard, H.C., 1960. Deformation of rocks at 500 °C to 800 °C. In: Griggs, D.T., Handin, J. (Eds.), Rock Deformation. Memoirs Geological Society of America, Boulder, CO, USA, pp. 39–104.
Handin, J., Hager, R.V., 1957. Experimental deformation of sedimentary rocks under confining pressure: tests at room temperature on dry samples. AAPG Bull. 41 (1), 1–50.
Head, D., Vanorio, T., 2016. Effects of changes in rock microstructures on permeability: 3-D printing investigation. Geophys. Res. Lett. 43, 7494–7502.
Heard, H.C., 1960. Transition from brittle to ductile flow in Solenhofen limestone as a function of temperature, confining pressure and interstitial fluid pressure. In: Rock Deformation (A Symposium). Geological Society of America, New York, USA, pp. 193–226.
Hebib, R., Belhai, D., Alloul, B., 2017. Estimation of uniaxial compressive strength of North Algeria sedimentary rocks using density, porosity, and Schmidt hardness. Arabian J. Geosci. 10 (383), 1–13.
Jaeger, J.C., Cook, N.G.W., Zimmerman, R.W., 2007. Fundamentals of Rock Mechanics, fourth ed. Blackwell Publishing Ltd., UK.

Jamshidi, A., Zamanian, H., Sahamieh, R.Z., 2017. The effect of density and porosity on the correlation between uniaxial compressive strength and p-wave velocity. Rock Mech. Rock Eng. 51, 1279–1286.
Jensen, L.R.D., Friis, H., Fundal, E., Møller, P., Jespersen, M., 2010. Analysis of limestone micromechanical properties by optical microscopy. Eng. Geol. 110 (3–4), 43–50.
Kovacik, J., 1999. Correlation between Young's modulus and porosity in porous Materials. J. Mater. Sci. Lett. 18, 1007–1010.
Kozeny, J., 1927. About Capillary Conduction of Water in the Soil (Ascent, Infiltration and Application to Irrigation), vol. 136. Academy of Sciences Meeting Report, Vienna, Austria, pp. 271–306 (in German).
Kranz, R.L., Frankel, A.D., Engelder, T., Scholz, C.H., 1979. The permeability of whole and jointed Barre Granite. Int. J. Rock Mech. Min. Sci. Geomech. Abstr. 16, 225–234.
Kurtulus, C., Cakir, S., Yoğurtcuoğlu, A.C., 2016. Ultrasonic study of limestone rock physical and mechanical properties. Soil Mech. Found. Eng. 52 (6), 348–354.
Lindsay, R.F., Cantrell, D.L., Hughes, G.W., Keith, T.H., Mueller III, H.W., Russel, S.D., 2006. Ghawar arab-D reservoir: widespread porosity in shoaling-upward carbonate cycles, Saudi Arabia. In: Harris, P.M., Weber, L.J. (Eds.), Giant Hydrocarbon Reservoirs of the World: from Rocks to Reservoir Characterization and Modelling, vol. 88. AAPG Memoir, pp. 97–137.
Logan, J.M., 1987. Porosity and the brittle-to-ductile transition in sedimentary rocks. AIP Conf. Proc. 154, 229–242.
Lucia, F.J., 1995. Rock-fabric/petrophysical classification of carbonate pore space for reservoir characterization. AAPG (Am. Assoc. Pet. Geol.) Bull. 79 (9), 1275–1300.
Maryam, H., Moradi, S., Fattahi, M., Zargar, G., Kamari, M., 2018. Estimation of rock uniaxial compressive strength for an Iranian carbonate oil reservoir: modeling vs. artificial neural network application. Prod. Res. 3, 336–345.
Mazzullo, S.J., 2004. Overview of porosity in carbonate reservoirs. Kansas Geol. Soc. Bull. 79, 412–422.
Mazzullo, S.J., Chilingarian, G.V., Bissell, H.J., 1992. Carbonate rock classification. In: Carbonate Reservoirs Characterization: A Geological-Engineering Analysis. Part 1. Elsevier, Amsterdam, Netherlands, pp. 59–108.
Mogi, K., 1967. Effect of the intermediate principal stress on rock failure. J. Geophys. Res. Solid Earth 72 (20), 5117–5131.
Mogi, K., 2007. Experimental Rock Mechanics, Geomechanics Research Series, vol. 3. Taylor and Francis, UK.
Moh'd, B.K., 2009. Compressive strength of Vuggy Oolitic Limestones as a function of their porosity and sound propagation. Jordan J. Earth Environ. Sci. 2, 18–25.
Moore, C.H., Wade, W.J., 2013. Natural fracturing in carbonate reservoirs. In: Carbonate Reservoirs, second ed. Elsevier B.V., Amsterdam, Netherlands (Chapter 11).
Najibi, A., Ghafoori, M., Lashkaripour, G.R., Asef, M.R., 2015. Empirical relations between strength and static and dynamic elastic properties of Asmari and Sarvak Limestones, two main oil reservoirs in Iran. J. Pet. Sci. Eng. 126, 78–82.
Nezamabadi, S., Radjai, F., Mora, S., Delenne, J., Chadiri, M., 2021. Rheology of soft granular Materials: uniaxial compression. Euro Phys. J. Web Conf. 249, 05008.
Nicolas, A., Fortin, J., Regnet, J.B., Dimanov, A., Geuguen, Y., 2016. Brittle and semi-brittle behaviours of a carbonate rock: influence of water and temperature. Geophys. J. Int. 206, 438–456.
Nur, A., Mavko, G., Dvorkin, J., 1998. Critical porosity: a key to relating physical properties to porosity in rocks. Lead. Edge 17 (3), 357–362.
Nicolas, A., Fortin, J., Regnet, J.B., Dimanov, A., Geuguen, Y., 2017. Brittle and semi-brittle creep of Tavel Limestone deformed at room temperature. J. Geophys. Res. Solid Earth 122, 4436–4459.
Ng, K.W., Sullivan, T.A., 2017. Case studies to demonstrate challenges of driven piles on rock. Geotech. Res. 4 (2), 82–93.
Ng, K.W., Yasrobi, S.Y., Sullivan, T.A., 2015. Current limitations and challenges with estimating resistance of driven piles on rock as demonstrated using three case studies in Wyoming. In: Proceedings of the International Foundations Congress & Equipment Exposition. Geotechnical Special Publication No. 256, San Antonio, TX, USA, pp. 500–517.
Ng, K.W., Yu, H., Kaszuba, J., Alvarado, V., Grana, D., Campbell, E., 2019. Geomechanical investigation of the carbon sequestration reservoir at Rock Springs Uplift, Wyoming, USA. In: Proceedings of the 53rd US Rock Mechanics/Geomechanics Symposium, New York, USA.
Palchik, V., 2010. Mechanical behavior of carbonate rocks at crack damage stress equal to uniaxial compressive strength. Rock Mech. Rock Eng. 43, 497–503.
Palchik, V., 2011. On the ratios between elastic modulus and uniaxial compressive strength of heterogeneous carbonate rocks. Rock Mech. Rock Eng. 44, 121–128.
Palchik, V., Hatzor, Y.H., 2000. Correlation between mechanical strength and microstructural parameters of dolomites and limestones in the Judea Group. Israel. Israel J. Earth Sci. 49, 65–79.
Palchik, V., Hatzor, Y.H., 2002. Crack damage stress as a composite function of porosity and elastic matrix stiffness in dolomites and limestones. Eng. Geol. 63, 233–245.
Paterson, M.S., Wong, T.F., 2005. Experimental Rock Deformation: the Brittle Field, second ed. Springer Verlag, Berlin, Germany.
Prasad, U., Curry, D., Hughes, B., Mohanty, B., Nasseri, M.H.B., 2009. Improved method for estimating the strength of carbonate rocks. In: Proceedings of the International Petroleum Technology Conference. Doha, Qatar. Paper IPTC 14043.
R Core Team, 2016. R: A Language and Environment for Statistical Computing. R Foundation for Statistical Computing, Vienna, Austria. http://www.R-project.org/. (Accessed 29 July 2022).
Ren, X.W., Santamarina, J.C., 2017. The hydraulic conductivity of sediments: a pore size perspective. Eng. Geol. 233, 48–54.
Renner, J., Rummel, F., 1996. The effect of experimental and microstructural parameters on the transition from brittle failure to cataclastic flow of carbonate rocks. Tectonophysics 258, 151–169.
Roehl, P.O., Choquette, P.W., 1985. Carbonate Petroleum Reservoirs. Springer, Berlin, Germany, pp. 1–15.
Rutter, E.H., 1972. The effects of strain-rate changes on the strength and ductility of Solenhofen limestone at low temperatures and confining pressures. Int. J. Rock Mech. 9, 183–189.
Rzhevsky, V., Novick, G., 1971. The Physics of Rocks. Mir Publishers, Moscow, Russia.
Sahimi, M., 1994. Applications of Percolation Theory, first ed. Taylor and Francis, CRC Press, London, UK.
Saller, A.H., Dickson, J.A.D., Boyd, S.A., 1994. Cycle stratigraphy and porosity in pennsylvanian and lower permian shelf limestones, eastern central basin platform, Texas. AAPG Bull. 78 (12), 1820–1842.
Sato, K., Kawakita, M., Kinoshita, S., 1981. The Dynamic Fracture Properties of Rock under Confining Pressure. Memoirs of the Faculty of Engineering, vol. 15. Hokkaido University, pp. 467–478.
Schwartz, A.E., 1964. Failure of rock in the triaxial shear test. In: Proceedings of the 6th U.S. Symposium on Rock Mechanics. Rolla, MO, USA, Paper No. ARMA-64-109, pp. 109–151.
Scott, T.E., 1989. The Effects of Porosity on the Mechanics of Faulting in Sandstones. PhD Thesis. University of Texas at Dallas, Richardson, TX, USA.
Serdengecti, S., Boozer, G.D., 1961. The effects of strain rate and temperature on the behavior of rocks subjected to triaxial compression. In: Proceedings of 4th U.S. Symposium of Rock Mechanics. University Park, Pennsylvania, USA, pp. 83–97.
Shafer, L., 2013. Assessing Injection Zone Fracture Permeability through the Identification of Critically Stressed Fractures at the Rock Springs Uplift CO_2 Sequestration Site, SW Wyoming. MSc Thesis. University of Wyoming, Laramie, WY, USA.
Shepherd, M., 2009. Carbonate reservoirs. In: Oil Field Production Geology, vol. 91. AAPG Memoir, pp. 301–309.
Summers, R., Winkler, K., Byerlee, J., 1978. Permeability changes during the flow of water through Westerly granite at temperatures of 100-400 °C. J. Geophys. Res. 83, 339–344.
Surdam, R., Jiao, Z., 2007. The Rock Springs Uplifts - an Outstanding Geological CO_2 Sequestration Site in Southwest Wyoming. Wyoming State Geological Survey, Challenges in Geologic Resource Development No. 2. Citizen Printing, Fort Collins, CO, USA.
Surdam, R., Bentley, R., Campbell-Stone, E., et al., 2013. Site Characterization of the Highest-Priority Geologic Formations for CO_2 Storage in Wyoming. Final report submitted to Department of Energy, Award Number DE-FE0002142, Carbon Management Institute, University of Wyoming, Laramie, WY, USA.
Ternero, F., Rosa, L.G., Urban, P., Montes, J.M., Cuevas, F.G., 2021. Influence of the total porosity on the properties of sintered materials-A review. Metals 11 (730), 1–21.
Tiab, D., Donaldson, E.C., 2012. Petrophysics: Theory and Practice of Measuring Reservoir Rock and Fluid Transport Properties, third ed. Gulf Professional Publishing, Boston, USA.
Turner, F.J., Griggs, D.T., Heard, H.C., 1954. Experimental deformation of calcite crystals. Geol. Soc. Am. Bull. 65, 883–934.
Vasarhelyi, B., 2005. Statistical analysis of the influence of water content on the strength of the Miocene limestone. Rock Mech. Rock Eng. 38 (1), 69–76.
Vajdova, V., Baud, P., Wong, T.F., 2004. Compaction, dilatancy, and failure in porous carbonate rocks. J. Geophys. Res. 109 (B05204), 1–16.
Vajdova, V., Baud, P., Wong, T.F., 2012. Micromechanics of inelastic compaction in two allochemical limestones. J. Struct. Geol. 43, 100–117.
Vanorio, T., Mavko, G., 2011. Laboratory measurements of the acoustic and transport properties of carbonate rocks and their link with the amount of microcrystalline matrix. Geophysics 76 (4), 1JA–Z99.
Vernik, L., Bruno, M., Bovberg, C., 1993. Empirical relations between compressive strength and porosity of siliclastic rocks. Int. J. Rock Mech. Min. Sci. Geomech. Abstr. 30 (7), 677–680.
Walton, G., Hedayat, A., Kim, E., Labrie, D., 2017. Post-yield strength and dilatancy evolution across the brittle-to-ductile transition in Indiana Limestone. Rock Mech. Rock Eng. 50, 1691–1710.
Wang, H., 2017. Nuclear Magnetic Resonance Studies of Rock Characterization in CO_2 Storage and Sequestration. PhD Thesis. University of Wyoming, Laramie, WY, USA.
Wang, H., Alvarado, V., Bagdonas, D., et al., 2021. Effect of CO_2-Brine and rock reactions on pore architecture and permeability in dolostone: implications for CO_2 storage and EOR. Int. J. Greenh. Gas Control 107, 103283.
Wong, T.F., Baud, P., 2012. The brittle-to-ductile transition in porous rock: a review. J. Struct. Geol. 44, 25–53.
Wong, T.F., David, C., Zhu, W., 1997. The transition from brittle faulting to cataclastic flow in porous sandstones: mechanical deformation. J. Geophys. Res. 102 (B2), 3009–3025.

Yu, H., 2018. Geotechnical Characterization of CO_2 Storage Reservoirs on the Rock Springs Uplift. PhD Thesis. University of Wyoming, Laramie, WY, USA.
Yu, H., Ng, K.W., Kaszuba, J., Campbell-Stone, E., Alvarado, V., Drana, D., 2019. Experimental investigation of the effect of compliant pores on reservoir rocks under hydrostatic and triaxial compression stress states. Can. Geotech. J. 56, 983–991.
Zarif, I.H., Tugrul, A., 2003. Aggregate properties of devonian limestones for use in concrete in istanbul, Turkey. Bull. Eng. Geol. Environ. 62, 379–388.
Zhu, W., Baud, P., Wong, T.F., 2010. Micromechanics of cataclastic pore collapse in limestone. J. Geophys. Res. 115, B04405.
Zoback, M.D., Byerlee, J.D., 1975. The effect of microcrack dilatancy on the permeability of Westerly granite. J. Geophys. Res. 80, 752–755.

Dr. Kam Ng obtained his BSc, MSc and PhD degrees in Civil Engineering from Iowa State University, USA. He had 10-year building consulting and construction experiences. He is currently an Associate Professor at University of Wyoming, and a Professional Engineer registered with the State of Wyoming, USA. His research focuses on transportation and energy geotechnics, and innovative building materials. He received the 2022 Samuel Hakes Outstanding Graduate Research and Teaching Award from the College of Engineering and Applied Science, 2022 Mid-Career Graduate Faculty Mentor Award from the University of Wyoming, 2013 Young Professor Paper Award, first runner-up, from the Deep Foundation Institute and 2012 Soil Mechanics Best Paper Award from the Transportation Research Board. He was the 2022 American Society of Civil Engineers Geo-Institute State-of-Practice Speaker. He published more than 85 papers and 20 technical reports and received more than 6.5 millions in research funding.